AD-A085 809 ARMY RESEARCH AND TECHNOLOGY LABS MOFFETT FIELD CA F/G 1/2
DYNAMIC STALL ON ADVANCED AIRFOIL SECTIONS,(U)
MAY 80 W J MCCROSKEY, K W MCALISTER, L W CARR

UNCLASSIFIED NL

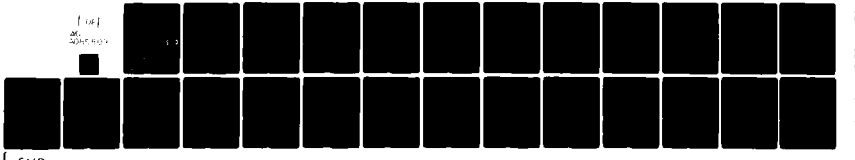

END
DATE FILMED
7-80
DTIC

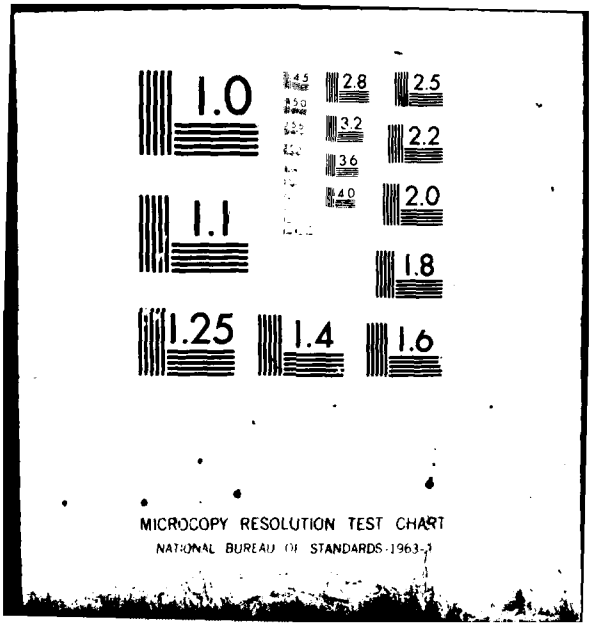
1.0
1.1
1.25
1.4
1.6
1.8
2.0
2.2
2.5
2.8
3.2
3.6
4.0
MICROCOPY RESOLUTION TEST CHART
NATIONAL BUREAU OF STANDARDS-1963-A

(6) Dynamic Stall on Advanced Airfoil Sections,

(10) W. J. McCroskey K. W. McAlister L. W. Carr and S. L. Pucci
Aeromechanics Laboratory
U.S. Army Research and Technology Laboratories (AVRADCOM)
Ames Research Center, Moffett Field, California 94035

J. J. Lambert
Service Technique des Constructions Aéronautiques
Paris, France

and

Lt. R. F. Indergand, USAF
Mather Air Force Base, California

(12) 26

PRESENTED AT THE 36TH ANNUAL FORUM
OF THE
AMERICAN HELICOPTER SOCIETY
WASHINGTON, D.C.
(11) MAY 1980

PREPRINT NO. 80-1

410540

Dynamic Stall on Advanced Airfoil Sections

W. J. McCroskey, K. W. McAlister, L. W. Carr, and S. L. Pucci
Aeromechanics Laboratory
U.S. Army Research and Technology Laboratories (AVRADCOM)
Ames Research Center, Moffett Field, California 94035

O. Lambert
Service Technique des Constructions Aéronautiques
Paris, France

and

Lt. R. F. Indergand, USAF
Mather Air Force Base, California

Abstract

The dynamic stall characteristics of eight airfoils have been investigated in sinusoidal pitch oscillations over a wide range of two-dimensional unsteady flow conditions. The results provide a unique comparison of the effects of section geometry in a simulated rotor environment. Important differences between the various airfoils were observed, particularly when the stall regimes were penetrated only slightly. Under these circumstances, the profiles that stall gradually from the trailing edge appear to offer an advantage. However, all of the airfoils tended increasingly toward leading-edge stall when both the severity of dynamic stall and the free-stream Mach number increased. In all cases, the parameters of the unsteady motion appear to be more important than airfoil geometry for configurations that are appropriate for helicopter rotors.

Introduction

Retreating-blade stall is a well-known limiting factor for the high-speed performance of most modern helicopters. In the past decade numerous new airfoil designs have been used in an attempt to improve the stall characteristics of rotors without compromising advancing-blade performance. Although the blade-element environment on the retreating side of the disc is highly unsteady, almost none of these new airfoils have been designed with dynamic-stall considerations in mind, and few of them have been tested under unsteady conditions in wind tunnels. Furthermore, the details of dynamic stall depend on a large number of parameters (Table 1), and the limited data sets that do exist have almost no overlap of the important parameters of the oscillatory motion.

Quantitative comparisons and assessments of new rotor-blade sections are further obscured by the effects of three-dimensional wind-tunnel interactions, wall interference, and experimental uncertainties. These are serious problems even for static stall, as indicated by the results plotted in Fig. 1 for two very different airfoils. The shaded band shows, for the classical NACA 0012, the spread of measured values of the maximum lift coefficient from our experiment and from those reported previously.[1-6] The symbols show the present measurements of $C_{L_{max}}$ for the Boeing-Vertol VR-7 airfoil, along with values from References 5-7. From this figure, we may conclude that the difference in stall characteristics from one wind tunnel to another can be the same order of magnitude as the differences between airfoil sections, and this factor must be considered when evaluating new rotor-blade sections.

The primary objective of the present investigation, then, was to fulfill the obvious need for a standard data base and to compare the basic dynamic-stall characteristics of a series of representative modern helicopter rotor airfoils. Figure 2 shows the eight sections that were tested under identical unsteady conditions in the same wind tunnel. Our second main objective was to investigate the type of stall and boundary-layer separation characteristics associated with each profile, since this was expected to be crucial in correlating the similarities and differences between different sections and in estimating the dynamic-stall behavior of new airfoils in the future. Another objective was to supplement the conventional lift and pitching moment measurements with unsteady form drag and stall flutter boundaries. Finally, we examined the effects of small amounts of leading-edge roughness, comparable to that due to erosion of blades operating in severe field conditions or due to incipient icing. The roughness also served to trip the boundary layer just ahead of the leading-edge laminar separation bubble that would have normally existed on the smooth airfoils.

In this paper, we present the highlights and principal results of the extensive data that were obtained on the eight airfoils. The complete program, consisting of static data sets obtained at four values of free-stream Mach number and unsteady data at an average of approximately 55 different conditions for each airfoil, will be documented in a forthcoming Army report.

Description of Experiment

The tests were performed in the U.S. Army 2- by 3-m atmospheric-pressure, solid-wall wind tunnel. The tests were conducted in essentially the same manner as in a previous experiment[8,9] except that the free-steam Mach number was extended to 0.3, the model chord c was reduced to 0.62 m, and the data processing was refined considerably. The models spanned the 2-m vertical dimension of the wind tunnel and were oscillated sinusoidally in pitch about the quarter chord, at frequencies up to 11 Hz. (Higher harmonic distortion of the motion was about 2% of the amplitude.) An improved version of the drive mechanism described in References 8 and 9 allowed both the mean angle α_0 and the frequency of oscillation ω to be varied continuously while the tunnel was operating. Discrete amplitudes of oscillation α_1 of 2°, 5°, 8°, 10°, or 14° could be set between runs.

The models of the eight airfoils, shown in Fig. 2 and Table 2, consisted of interchangeable shells constructed of wood and fiberglass surrounding a stainless steel spar that contained the instrumentation and wiring. Each set of shells was precision-machined, while mounted on the spar, to a design accuracy of ±0.1 mm. However, measurements after the test revealed that the rms standard deviation of the contour errors was about 0.4 mm, or 0.06% of chord, and that the maximum error was 0.85 mm.

Instrumentation

The primary data were obtained from 26 Kulite differential pressure transducers, types YQCH-250-1 and YQCL-093-15. The transducers were distributed over the upper and lower surfaces, with seven of them concentrated in the leading-edge region ($x/c \leq 0.05$) and two near the trailing edge (at $x/c = 0.98$); they were referenced to the total pressure in the wind tunnel.

Surface hot films and boundary-layer hot-wire probes were installed at six locations on the upper surface to determine the boundary-layer transition, flow reversal, and separation characteristics.[9,14] In addition, a hot-wire probe protruding just outside the boundary layer was mounted near the leading edge of the NLR-1 profile to aid in diagnosing the local supersonic zone that was frequently observed at high incidence. A shadowgraph system was also used to visualize the transonic flow in this region. Finally, a traversing pitot-static probe was used to survey the wake and determine the drag of each airfoil under steady flow conditions.

Data Analysis and Measurement Accuracy

The pressure transducer and hot-wire signals were amplified and recorded on a 32-channel analog tape recorder, along with the average free-stream dynamic pressure, the instantaneous angle of attack of the model, and 1/cycle and 200/cycle timing indicators. These data tapes were digitized and ensemble-averaged off-line, during which at least 50 cycles of data were sampled 200 times per cycle. The averaged pressure data were then processed and integrated numerically by trapezoidal rule to determine the unsteady lift, moment, and pressure drag. On the other hand, individual cycles of the analog hot-wire and hot-film records were examined to determine the boundary-layer characteristics, as discussed in References 9, 14, and 15.

Special on-line analog computers that calculated and displayed the instantaneous normal force, pitching moment, pitch damping, and pressure distributions proved to be extremely valuable in assessing the dynamic-stall behavior, as well as the performance of the instrumentation, as the tests were in progress. These devices also enabled us to vary the unsteady parameters until some desired result was obtained, such as the maximum lift condition in the absence of moment stall or neutral aerodynamic damping in pitch.

For the present purpose of comparing the dynamic-stall characteristics of the eight airfoil sections, the absolute accuracy of the measurements is less important than the random experimental errors, but we have attempted to assess both. Based on the method of Allen and Vincenti,[16] static wind-tunnel wall corrections below stall amount to about 1% for α and about 1.5% for C_L; these and a 1% correction due to a reduction in test section area at the model have been applied to the static data shown in Fig. 1 and Table 3, but not to the dynamic data. Fromme and Golberg[17] have indicated that

unsteady wall corrections can be greater than the corresponding static corrections, but it is not clear to what extent their potential flow analysis can be applied to the present measurements. Likewise, we have not been able to establish estimates of the poststall tunnel sidewall effects, but tuft flow visualization and previous experience suggest that these problems become less important as the frequency of oscillation increases.

The maximum error of the angular measurements is estimated to be ±0.2°, and that of the frequency of oscillation ±0.03 Hz. The uncertainty in the pressure, force, and moment coefficients depends on the operating conditions. For example, the probable error in C_D is estimated to vary from less than ±0.05 at $M_\infty = 0.3$ and $\alpha = 0$ to about ±0.5 at $M_\infty = 0.1$ and α approaching the stall angle. For the static data presented in this paper, the measurement uncertainty is estimated at ±0.03 for $C_{L_{max}}$, ±0.005 for C_M, and ±0.0005 for C_D. The uncertainty in the SC-1095 static lift data is about 2 times larger, because of some unresolved difficulties with the static pressure measurements. The unsteady data in the dynamic-stall regime should be in error by no more than ±0.10 for C_L, and ±0.025 for C_M and C_D.

Test Conditions

The primary reference conditions for the initial comparisons of the various airfoils were static and deep dynamic stall at $M_\infty = 0.30$, with the unsteady motion given by $\alpha = 10° + 10° \sin \omega t$ and $k = \omega c/2U_\infty = 0.10$. Limited, but systematic variations in Mach number and the unsteady parameters were explored as follows: (1) static data at discrete values of α for $M_\infty = 0.11$, 0.185, 0.25, and 0.30; (2) unsteady data with $\alpha = 15° + 10° \sin \omega t$ and $k = 0.10$ for $M_\infty = 0.076$, 0.11, 0.185, 0.22, 0.25, 0.28, and 0.295; (3) frequency sweeps at $M_\infty = 0.30$ with $0.01 \le k \le 0.20$, $\alpha_0 = 10°$ and 15°, and $\alpha_1 = 5°$ and 10°; (4) variations in α_0 to obtain the maximum lift for each airfoil without moment stall at $M_\infty = 0.30$ with $\alpha_1 = 10°$ and $k = 0.10$; (5) at $M_\infty = 0.185$ and 0.30 with $\alpha_1 = 10°$, variations in α_0 for each airfoil so that α_{max} is slightly greater than the static stall angle and dynamic stall occurs at low frequencies but possibly disappears as k increases; (6) variations in both α_0 and k at $M_\infty = 0.3$ with $\alpha_1 = 2°$, to obtain boundaries of neutral aerodynamic damping in pitch and to obtain the maximum negative value of the pitch damping parameter, $\zeta = -\oint C_M d\alpha/4\alpha_1^2$; and (7) duplication of some of the test conditions of References 8, 18-20.

A limited amount of static and dynamic data were obtained on each airfoil at M = 0.185 and 0.30 with a boundary-layer trip, consisting of a 3-mm-wide band of 0.10-mm-diameter glass spheres glued to the leading edge. As mentioned in the Introduction, this trip eliminated the laminar separation bubble that would normally form near the leading edge as the stall angle was approached, and it also roughly simulated severe field conditions of many helicopters.

Finally, it should be mentioned that the variation in Reynolds number with Mach number was $Re \approx 14 \times 10^6 M_\infty$.

Discussion of the Unsteady Flow Phenomena

Many of the qualitative features that distinguish dynamic stall from static stall are approximately the same for a wide range of airfoil shapes and ambient flow conditions, and the basic stall behavior is strongly influenced by the three main phenomena described below.

Vortex Shedding and Degree of Stall

Numerous experiments have shown that dynamic stall is characterized by the shedding and convection over the upper surface of the airfoil of a vortex-like disturbance, which induces a highly nonlinear, fluctuating pressure field. If the reduced frequency, amplitude, and maximum incidence are sufficiently high, the vortex-shedding phenomenon is well defined, the unsteady fluctuations in the airloads are very large, and the qualitative results are relatively independent of airfoil shape, Reynolds number, and type of motion. We shall call this limiting case "deep dynamic stall"; it corresponds to the "fully-developed" vortex, or vortex-dominated, cases that were analyzed previously.[8,9,15]

Under the less severe conditions that are more common in helicopter applications, the vortex-shedding phenomenon is less well defined. The origin, strength, and transient development of the vortex, and even the qualitative behavior of the airloads, appear to depend on all the parameters listed in Table 1. The airloads typically exhibit significant amounts of hysteresis, and negative aerodynamic damping is more likely to occur than in deep stall, but the maximum values of the force and moment coefficients generally remain in the same range as their static counterparts. This we shall call "light dynamic stall."

The boundary between light and deep dynamic stall is rather broad and somewhat arbitrary, of course. However, we can see the evolution of the different types of stall behavior in Figs. 3 and 4, which show the effects of variations in the mean angle for the NACA 0012 airfoil.

For the lowest value of α_o, the maximum angle of attack is less than the static-stall angle of 13.7°, the boundary layer remains attached throughout the cycle, and the flow can be roughly approximated by classical inviscid theory. For $\alpha_o \approx 4°$ under the conditions shown in Fig. 3, the boundary layer separates over the rear half of the airfoil during the downstroke, and this produces distortions in the pitching-moment loop that are comparable in magnitude to the unsteady inviscid effects. This important condition, which we call "stall onset," represents the limiting case of maximum lift with no penalty in C_M or C_D. It is the unsteady counterpart for helicopter applications to operating a fixed wing just on the verge of stall, and therefore it represents a measure of the maximum useful lift that a given airfoil can deliver if drag-rise and moment stall are to be avoided.

Using the behavior of C_M as a criterion, we have found the progression from stall onset to light stall to be rather abrupt and well defined for all of the helicopter airfoils, as α_o was increased in small increments. For the NACA 0012, light stall was evident at $\alpha_o \approx 5°$ for the conditions shown in Fig. 3. Moment stall (denoted by M in the figure) occurred fairly abruptly when the boundary layer separated near α_{max}; this was followed by a negative contribution to the net aerodynamic pitch damping during the initial part of the downstroke. Although the pressure transducers indicated a weak vortex peak originating at $x/c \approx 0.05$, it did not appear to cause the airloads to be significantly different from the static case. Also, the loss in lift on the downstroke occurred gradually and was a small fraction of $C_{L_{max}}$.

On the other hand, the vortex becomes very important entering the deep-stall regime, shown in the right-hand part of Fig. 3. The vortex originates even closer to the leading edge just prior to moment stall M and produces a large negative pitching moment, high drag, and an additional increment in lift as it passes over the airfoil. (Lift stall is denoted by L.) The dramatic changes in the shape and magnitude of the hysteresis loops of C_L, C_M, and C_D from the preceding cases resemble closely what was observed in References 8 and 9 at lower Mach number, although the lift coefficient rose to greater peak values during the vortex shedding process in our earlier tests. This was apparently due to greater suction being maintained at the leading edge during the early stages of dynamic stall. These differences in the collapse of the leading-edge suction, which appear to depend on Mach number and airfoil geometry, are still under study.

Further increases in α_o (or in k at the same values of α_o and α_1) produce additional increases in the vortex strength and in the peak values of the airloads. Variations in the time histories of the aerodynamic coefficients occur, and the phase in the cycle for boundary-layer separation and reattachment also continue to change. This is reflected in varying hysteresis loops of C_L, C_M, and C_D versus α; however, the basic phenomenon remains approximately the same (cf. Ref. 9). This is illustrated in Fig. 4, which shows the waveforms of C_M versus ωt. As before, L and M denote lift stall and moment stall, respectively, and R signifies complete boundary-layer reattachment. This alternative format shows the similarities between the deep-stall cases and their differences with respect to light stall. Also evident is the development of a secondary vortex that becomes rather pronounced at $\omega t \approx \pi/3$ for $\alpha_o = 20°$. This secondary vortex was evident in varying degrees on several of the other airfoils, particularly on the VR-7.

Leading-Edge vs Trailing-Edge Stall

A second characteristic that strongly influences the dynamic stall behavior, especially in the light-stall regime, is the nature of the initial boundary-layer separation that precedes the vortex development. The conventional categories of stall on static airfoils are leading-edge, thin-airfoil, and trailing-edge stall, with the first of these generally ascribed to all airfoils that stall abruptly.[21] Leading-edge stall, which is the category that is the least understood and the most difficult to control or predict, is generally associated with the bursting of a laminar leading-edge separation bubble. The term trailing-edge stall is commonly applied to airfoils that exhibit boundary-layer separation that progresses gradually forward as the angle of attack increases.

In References 9 and 15, however, we established that leading-edge stall could be due either to the bursting of a leading-edge laminar separation bubble and subsequent rearward motion of an expanding separation zone or to the abrupt forward propagation of turbulent

separation that began as trailing-edge stall. In the present investigation, we discovered still another mechanism for leading-edge stall and, in addition, a flow breakdown that progressed both upstream and downstream from a midchord point of initial boundary-layer separation. Hence the nomenclature, as well as the phenomena, has become rather confusing. We shall try to clarify the picture in the following examples.

Trailing-Edge Stall. The classical picture of gradual trailing-edge separation was observed on the NLR-7301 airfoil under both static and dynamic conditions. The latter is illustrated in Fig. 5, where the time histories of the pressure are displayed in the manner suggested by Carta,[22] along with the boundary-layer separation and reattachment behavior. In the unsteady case shown on the NLR-7301, moment stall is preceded by a gradual forward movement of flow reversal in a thin layer at the bottom of the boundary layer. When this flow reversal reaches the leading-edge region, stall begins gradually, and a vortex forms at $x/c \approx 0.3$ and moves rearward over the airfoil.

Leading-Edge Stall. In contrast to the trailing-edge stall behavior, the initial breakdown of the flow on the NLR-1 airfoil began somewhere between the hot films at $x/c = 0.026$ and 0.10, and this flow separation disturbance moved rearward. A vortex appeared virtually simultaneously; it appeared in the pressure signals as far forward as $x/c = 0.011$ and followed closely behind the boundary-layer disturbance. The moment stall was much more abrupt in this case. Similar behavior was observed on the NACA 0012 and Wortmann 098 under these test conditions.

Unlike our previous observations[9,15] at lower Mach number, the rearward-spreading flow breakdown on these profiles clearly originated in the turbulent part of the boundary layer. Evidently the laminar separation bubble just upstream of the turbulent separation played no significant role in this process, because the leading-edge trip eliminated it with hardly any effect on the results. The turbulent separation that we observed previously[9,15] always appeared to propagate from the rear forward, either gradually or very suddenly, depending on the leading-edge geometry. The sudden cases we now propose to call "abrupt trailing-edge stall," to distinguish them from the cases of boundary-layer disturbances that travel downstream from the leading-edge region; throughout the remainder of this paper the term "leading-edge stall" will only be applied to cases where the boundary layer initially separates, or breaks down catastrophically, in the leading-edge region, forward of $x/c \approx 0.05$. Therefore, some cases that would normally be defined as leading-edge stall on the conventional basis[21] of an abrupt loss in lift will be classified as abrupt trailing-edge stall. If the trailing-edge separation is gradual, as on the NLR-7301, we will merely refer to it as trailing-edge stall.

Mixed Stall Behavior. A third case (Fig. 5) obtained on the VR-7 section represents a combination of leading-edge and trailing-edge stall. At low Mach number in the deep-stall regime, at all Mach numbers in the light-stall regime, and under all static conditions, this airfoil exhibited the gradual trailing-edge stall that is shown for the NLR-7301. However, for $M \geq 0.25$, a major boundary-layer disturbance and a vortex erupted out of the leading-edge region while the tongue of reversed flow on the rear half of the airfoil was moving forward; only sometime later did the two distinct boundary-layer disturbances appear to meet and merge somewhere near midchord. This phenomenon, which was even more pronounced on the VR-7 at $M_\infty = 0.28$ and 0.3 (and on the HH-02 for $M_\infty \geq 0.22$), is shown by the loci of flow reversal in the left-hand part of Fig. 6.

Another mixed stall case, also illustrated in Figs. 5 and 6, was observed on the Ames-01 and SC-1095 airfoils in the deep-stall regime for $M_\infty \leq 0.25$ and on the NLR-1 airfoil at lower Mach number. The first indications of boundary-layer separation were observed on the hot film at $x/c = 0.25$, with the disturbance spreading upstream and downstream from that general area. The vortex appeared to originate at $x/c \approx 0.17$ and to proceed downstream, as shown in the figure. Moment stall tended to be somewhat less abrupt than for the leading-edge stall cases. For $M_\infty \geq 0.28$, the boundary layer separation changed to a leading-edge origin, similar to the NLR-1 behavior.

These widely different types of boundary-layer separation represent formidable challenges to the theoretical analysis of dynamic stall, but what are the practical consequences? For deep stall at $M_\infty = 0.3$, all of the helicopter sections show a strong tendency toward leading-edge stall, and, as we shall see in subsequent sections, their aerodynamic behavior is very similar. The major differences in the unsteady airloads show up at stall onset and in the light-stall regime, where the boundary-layer characteristics differ the most. Before comparing the aerodynamic performance of the

various airfoils, however, let us discuss another phenomenon which seems to be related to the changes in the separation behavior that occur as the Mach number increases.

Transonic Flow Near the Leading Edge

Although several authors[5,23-25] have discussed the effects of Mach number on dynamic stall, little has been published about the supersonic flow that can develop near the leading edge at high angle of attack in a subsonic free stream. This becomes particularly interesting in unsteady conditions, since the stall can be delayed to very large angles of attack, and the leading-edge flow accelerated to local velocities much greater than U_∞. A simple extrapolation of previous results for $M_\infty < 0.1$ to the present conditions would predict hypersonic flow locally, so it is obvious that something must change as M_∞ increases.

To assess the actual situation, we used the steady isentropic flow relations to convert our leading-edge pressure measurements to local Mach number, and then looked for the maximum values that occurred just before the onset of stall. These peak values are plotted in Fig. 7 for a range of free-stream Mach numbers. The inset plot shows a representative instantaneous leading-edge pressure distribution, obtained on the NACA 0012, at $\alpha = 16.7°$ and $M_\infty = 0.295$.

The results in Fig. 7 clearly indicate the development of transonic flow near the leading edge for $M_\infty \geq 0.18$. As suggested by the plot of C_p versus x, the spatial extent of the supersonic zone was generally less than 2% of the chord, but it persisted for time intervals that represented several chord lengths of travel. As we shall see in later sections, the onset of supercritical flow corresponds approximately to the conditions for which most of the airfoils began to show a decrease in dynamic $C_{L_{max}}$ with increasing M_∞. Furthermore, the growth in the maximum local Mach number above sonic conditions was found to accompany a strong tendency toward leading-edge stall on all of the airfoils, whatever their behavior at low Mach number.

Another interesting feature of the leading-edge supersonic flow was the complete absence of shock waves, despite values of M_{max} that were estimated to be in excess of 1.4 in several cases. Further increases in M_∞ above our experimental limit of 0.30 would certainly be expected to produce some kind of shock-induced leading-edge stall,[5,12,26] but this does not seem to be the mechanism involved in the cases described in this paper. The evolution of shock stall at $M_\infty > 0.3$ and the details of its influence on the unsteady airloads are important topics for further research.

Comparison of Results

We turn our attention now to the variations in aerodynamic behavior that were observed on the eight airfoils over the range of test conditions of the experiment.

Static Data

The measurements performed under steady or quasi-static flow conditions provide a frame of reference for the dynamic stall results and a basis for comparison with data from other wind tunnels. Table 3 presents a summary of the primary characteristics of each airfoil at $M_\infty = 0.30$, where the subscript o refers to zero lift and α_{ss} is the angle for $C_{L_{max}}$. Also included are the calculations of drag-divergence Mach number at zero lift obtained from a nonconservative inviscid transonic flow code called FL06,[27] which is well suited to comparative studies of this type.

It is interesting to note that the four airfoils that were designed to optimize the compromise between retreating- and advancing-blade requirements (see Table 2) have approximately the same values of $C_{L_{max}}$ and M_{DD_o}. However, the Wortmann 098 and SC-1095 airfoils have significant negative values of pitching moment at low lift. The reduction of C_{M_o} by means of a trailing-edge tab to the levels of the Ames-01 and HH-02 profiles would probably result in reductions in $C_{L_{max}}$ by 0.05 to 0.08, based on the information in References 2, 5, and 12.

The NLR-7301 profile has the largest value of $C_{L_{max}}$, but it also has very large negative pitching moments, since it was not designed for helicopter conditions. Overall, the airfoils with the highest lift tend to have the lowest drag-divergence Mach numbers and vice versa, as would be expected.

Of the measured quantities listed in Table 3, only the stall angle and $C_{L_{max}}$ varied significantly with tunnel speed. Figure 8, which displays uncorrected data, shows that this effect is most pronounced on the NACA 0012 and NLR-1 airfoils. In general, we attribute the variations below $M_\infty \approx 0.2$ to Reynolds number effects and those above to Mach number effects. In any case, a comparison of the static results in Figs. 1 and 8 serves to reiterate our remarks in the Introduction regarding comparisons between airfoils versus comparisons between results from different wind tunnels.

Dynamic-Stall Onset

This condition, which was described earlier in connection with Fig. 3, represents the maximum stall-free lift that can be obtained under unsteady conditions. Figure 9 shows the values of $C_{L_{max}}$ at stall onset measured at $M_\infty = 0.3$ and $k = 0.10$ for large-amplitude oscillations, with no wind-tunnel wall corrections applied. All of the airfoils except the NLR-7301 show significant increases in $C_{L_{max}}$ over the corresponding uncorrected static values, with the greatest unsteady benefits accruing for the Ames-01 and VR-7 airfoils. Although unsteady wind-tunnel wall corrections[17] might reduce the actual magnitudes of $\Delta C_{L_{max}}$ somewhat, the dynamic stall angle for each helicopter section was larger than the static-stall angle; therefore, favorable performance increments can be expected in practical applications. At $k = 0.10$, however, the NLR-7301 airfoil could not be taken to within 2° of the static-stall angle without light dynamic stall occurring on the downstroke. Therefore, this profile suffered a slight performance loss due to unsteady effects.

These increments in unsteady lift, which depend significantly on airfoil shape, are a direct consequence of the unsteady effects on the boundary-layer separation characteristics. For the pitch oscillations indicated in Fig. 9, all of the airfoils stalled from the trailing edge, for reduced frequencies from 0.10 down to 0.01. The extent and abruptness of the separation varied considerably, and the quasi-static behavior was not necessarily a reliable guide to the dynamic-stall-onset characteristics. For example, the Ames-01 airfoil stalled abruptly between 13.5° and 14° at very low frequency, but at $k = 0.10$ the flow separated gently over no more than half of the model; this occurred on the downstroke well after the maximum incidence of 15.6° was attained. On the other hand, the HH-02 stalled rather gradually under quasi-static conditions, but tended to stall more abruptly as the frequency was increased. Its dynamic increment in $C_{L_{max}}$ at $k = 0.10$ was about two-thirds of that of the Ames-01 and about half that of the VR-7, which had a very gradual trailing-edge stall under these conditions.

This part of the experiment should provide a useful test of unsteady airfoil calculations. The separation was limited to the rear portions of the airfoils and to a small fraction of the cycle, and thus it should be much easier to model theoretically than deep stall. However, the results varied considerably from one airfoil to another, and a calculation method would have to predict these differences in order to be valid.

Light Stall Results

The unsteady aerodynamic behavior also tended to be sensitive to airfoil geometry in the light-stall regime. The boundary-layer separation was highly variable, and we observed a wide range of stall types as reduced frequency, amplitude, and mean angle were varied on the different profiles. Most of this part of the experimental program was restricted to $M_\infty = 0.30$ and $\alpha_1 = 5°$.

Figure 10 illustrates how widely the aerodynamic coefficients can vary for one set of unsteady conditions. In this example, the maximum incidence, 15°, was more than 1° greater than the static stall angle of all the profiles (cf. Table 3), except the NLR-7301. Consequently, all of the helicopter airfoils exhibited some dynamic overshoot of static $C_{L_{max}}$. The salient characteristics of each airfoil are described below.

For the NACA 0012, the maximum value of the lift coefficient in Fig. 10 is greater than static $C_{L_{max}}$ by an increment of 0.20; this was accompanied by dynamic $C_{M_{min}} \approx -0.09$ and a net aerodynamic damping in pitch that was slightly negative. The boundary-layer separation in this case progressed rapidly from the trailing edge. As α increased to 12° or as k increased to 0.20, this changed to leading-edge stall.

The Ames-01 airfoil had a slight amount of trailing-edge separation and approached stall onset for the conditions of Fig. 10. An increase in α_0 of 1° produced light stall qualitatively similar to the results shown for the NACA 0012.

The Wortmann 098 section exhibited a mixed boundary-layer separation that started out from the trailing edge but later broke sharply from $x/c \approx 0.10$. This behavior is apparently the cause of the sharp negative spike in C_M for the conditions shown in Fig. 10; it represents a transition between trailing-edge stall at lower reduced frequencies and leading-edge stall at larger k. Over the range $0.025 \leq k \leq 0.20$, this airfoil produced significantly larger pitching moments than any of the others.

The Sikorsky SC-1095 profile showed a somewhat greater tendency toward negative pitch damping than the others for the conditions shown in the figure and at other reduced frequencies. We failed to record the boundary-layer data for this case, but the leading-edge separation that we observed for $\alpha_0 = 11°$ is probably representative of $\alpha_0 = 10°$. This contrasts

with the quasi-steady mixed-stall behavior, where the initial flow breakdown occurred at $x/c \approx 0.25$ and spread in either direction. This unusual type of separation was also observed on the Ames-01 and NLR-1 under different test conditions, as discussed earlier in connection with Figs. 5 and 6.

The Hughes HH-02 airfoil made a striking change from a very gradual trailing-edge stall to a sharp leading-edge stall as k was increased from 0.025 to 0.10, where vortex shedding began to originate at $x/c \approx 0.05$. This changing behavior was very pronounced at other mean angles and amplitudes as well, for all Mach numbers above 0.2.

The Vertol VR-7 airfoil developed $C_{L_{max}} = 1.77$, second only to the NLR-7301 for the conditions of Fig. 10, with a gradual trailing-edge separation over the rear 40% of the airfoil and benign pitching moment behavior. Further increases in k suppressed the trailing-edge separation even more, reducing $C_{M_{min}}$ slightly and increasing $C_{L_{max}}$ to 1.87 at k = 0.20. However, increasing the mean angle to 15° produced dramatic changes in the stall behavior as a function of reduced frequency, including a transition from light stall to deep stall. We shall discuss this case in more detail in a later section of the paper.

The NLR-1 section, which stalled abruptly from the trailing edge under quasi-static conditions, changed to leading-edge stall for the conditions shown in Fig. 10. Due to its relatively low static-stall angle of 12.3° it began to stall somewhat earlier than the other airfoils. Moment stall was as abrupt as on the Wortmann 098, although the magnitude of the negative C_M spike was less.

Stall would not be expected on the last airfoil in the group, the NLR-7301, since its static-stall angle was almost 3° greater than α_{max}; this is confirmed by the results shown in the figure. It is noteworthy, however, that viscous effects served to reverse the sense of the $C_L - \alpha$ loop from the counterclockwise direction observed at lower mean angles (cf. Fig. 3). When the mean angle was increased to 15°, the stall changed from a gentle trailing-edge separation for $k \leq 0.05$ to a mixed leading- and trailing-edge type for $k \geq 0.15$. This change was rather similar to that of the VR-7, although the vortex was not as fully developed on the NLR-7301.

The preceding examples are representative of the broad panorama of dynamic stall behavior that can occur as conditions change from quasi-steady to deep-stall conditions. The common aspect of all of the light-stall data is that this regime represents a transition from static behavior, which can vary significantly from one airfoil to another, to deep stall, where the behavior is dominated by the dynamic stall vortex.

Deep-Stall Results

The differences between airfoils tend to be diminished in deep stall, where the vortex shedding phenomenon becomes fully developed. Figure 11 shows the hysteresis loops of C_L, C_M, and C_D versus α for the same airfoils and test conditions as Fig. 5; that is, representing four different types of boundary-layer separation. The results for the three helicopter sections are remarkably similar, differing principally in the angle for the onset of stall, in the magnitude of the peak forces and moments, and in the strength of the secondary vortex at the top of the cycle. The same could be said of the other four airfoils, not shown. All developed local Mach numbers well in excess of 1.0 just before moment stall began, and all developed force and moment coefficients greatly exceeding their static counterparts.

Effects of Mach Number. The deep-stall dynamic airloads for the unsteady motion indicated in Fig. 11 were also qualitatively the same at other values of M_∞. However, the actual peak values and the stall angles were found to depend somewhat on Mach number, as Fig. 12 illustrates for $C_{L_{max}}$. The static data from Fig. 8 are also shown for reference. It is interesting to note that the dynamic data generally decrease faster with increasing M_∞ than do the static data, and that the airfoils with higher values of dynamic $C_{L_{max}}$ are not necessarily the same as the ones with the higher static values. That is, the incremental $\Delta C_{L_{max}}$ above the static value depends on both Mach number and airfoil shape. The latter effect is shown in Fig. 13 for $M_\infty = 0.295$.

A wide range of boundary-layer separation characteristics is associated with the various unsteady data points in Figs. 12 and 13. For example, the VR-7 airfoil changed from trailing-edge to leading-edge stall and the Ames-01 changed from mid-chord separation to leading-edge stall between $M_\infty = 0.185$ and 0.295, as shown in Fig. 6. But, the general nature of the unsteady airloads changed very little over this range of Mach number; this indicates that the overall effects of the vortex-shedding phenomenon in deep stall are relatively independent of the details of the boundary-layer separation.

Effects of Reduced Frequency and Amplitude. These two parameters of the

unsteady motion, along with the mean angle, are the most important ones in determining the phase and strength of the vortex shedding characteristics in the deep-stall regime. Figure 14 illustrates the evolution of the phenomenon with reduced frequency for the VR-7 airfoil. The case with $k = 0.025$ corresponds to light stall, with maximum force and moment coefficients only slightly greater than the corresponding static values, whereas the effects of vortex shedding begin to show up at $k \approx 0.05$. Further increases in k produce a progressive transition to deep-stall behavior at $k = 0.20$. The changing strength of the vortex is also evident in the pressure distributions shown in Fig. 15 for $k = 0.05$ and 0.20.

The development of deep stall in this example involves a dramatic change in the boundary-layer separation characteristics, as shown in Fig. 16. At the three lower reduced frequencies, the stall is gradual, boundary-layer flow reversal progresses slowly upstream from the trailing edge, and a weak vortex originates around midchord. However, Fig. 16 shows a conversion to leading-edge stall between $k = 0.10$ and 0.20, and at the latter reduced frequency a much stronger vortex originated at $x/c \approx 0.025$. As we have noted before, deep-stall separation originated near the leading edge on all of the helicopter airfoils for $M_\infty > 0.25$, whatever their light-stall or low Mach-number behavior.

The hysteresis loops in Figs. 11 and 14 look very different, but there is a similarity in the airloads that can be highlighted if we consider the $\alpha(t)$ history of various motions. Figure 17 shows two cases that have very different amplitudes and reduced frequencies but identical mean angles and maximum pitch rates; that is, the product $\alpha_1 k$ is constant. The waveforms are plotted versus nondimensional time, or chordlengths of travel, and the curves are phased so that the angles of attack approximately overlap at the static stall angle α_{ss} on the upstroke.

We see that the airfoils stall at approximately the same angles and pitch rates and that the waveforms of C_L and C_M versus $U_\infty t/c$ are much more similar than are the hysteresis loops of C_L and C_M versus α. This comparison suggests that amplitude and reduced frequency are less important parameters in deep stall than α and its rate of change on the upstroke and that the dynamic-stall events proceed on a time scale $U_\infty t/c$ rather than ωt.

A significant improvement in matching different sets of data is shown in Fig. 18. Here the reduced frequency is lowered to 0.15 for the low amplitude case and the mean angle is 10° for $\alpha_1 = 10°$. Now the product $\alpha_1 k^2$, which is proportional to the maximum value of $\ddot{\alpha}$, is approximately constant, and the $\alpha(t)$ histories are nearly the same over the entire portion of the cycle for which $\alpha > \alpha_{ss}$. Although the pitch rates are different at α_{ss}, they are approximately the same at $\alpha = 17°$, which is about where moment stall begins. In these two cases, the lift and moment data are almost indistinguishable on the upstroke and throughout most of the stall events, whether viewed versus $U_\infty t/c$ or versus α. In fact, it is the behavior after the primary vortex passes off the airfoil that accounts for most of the differences between the four cases, Figs. 17 and 18.

Although there are definite limits to the procedures described above, the results in Figs. 17 and 18 are not isolated examples. A number of comparisons for other airfoils, amplitudes, and reduced frequencies in the deep-stall regime yielded comparable results; namely, the better the match between the $\alpha(t)$ histories between α_{ss}, α_{max}, and $\alpha_{reattachment}$, the better the match between the aerodynamic coefficients. Perhaps this conclusion will serve to stimulate new ideas for improved dynamic-stall correlation and prediction methods.

Effects of Leading-Edge Roughness. The strong tendency toward leading-edge separation in the deep stall regime raises the question of the role of the leading-edge laminar separation bubble in initiating the vortex shedding phenomenon. As in our earlier work,[8,9,15] the use of leading-edge roughness to trip the boundary layer just upstream of the bubble, thereby eliminating it, provided additional confirmation of our interpretation of the hot-wire and pressure measurements on the smooth airfoils. The result was that we observed no significant changes in either the static or deep dynamic stall characteristics of any of the helicopter sections. The stall angle and maximum values of lift were reduced slightly in some cases, but there was no change in the qualitative stall behavior. The reductions in $C_{L_{max}}$ that did occur tended to be greater at $M_\infty = 0.185$. Therefore, we may conclude that the observed leading-edge stall originated in the turbulent boundary layer a short distance downstream of the leading edge, and not with the bursting of the leading-edge laminar bubble, as proposed by Gault.[21]

Pitch Damping Boundaries

One of the adverse effects of dynamic stall is the possibility of negative aerodynamic damping in pitch, which could lead to single-degree-of-freedom stall flutter of an elastic blade. Since this important

characteristic turned out to vary considerably from one airfoil to another, we made a special study of it for small amplitude oscillations by mapping out the stability boundaries as a function of reduced frequency and mean angle. The results are shown in Fig. 19, where the shaded regions denote negative pitch damping and the crosshatched bands indicate the conditions for which the damping was approximately zero. Also shown for reference is the static-stall angle for each profile.

It is interesting to note that all of the airfoils are susceptible to instabilities over the entire range of frequencies studied for some values of α_0. Also noteworthy is that the left boundary was very distinct in each case; it corresponded to what we have called light stall. At high reduced frequency, this light stall began in the leading-edge region for the Wortmann 098 and NLR-1 airfoils and at $x/c \approx 0.25$ for the SC-1095. This behavior apparently leads to negative damping for values of α_{max} that are only slightly greater than the static-stall angle and to a relatively large domain of instability.

In contrast, the VR-7 stalled from the trailing edge for most of the conditions near or inside the unstable region. This produced a more narrow range of instability and a tendency for the boundaries to be delayed to larger angles of attack as k increased. However, the magnitude of the damping parameter ζ inside the unstable regime was as large as that of the other airfoils. The Ames-01 airfoil also stalled from the trailing edge, although somewhat more abruptly than the VR-7, and its domain of instability is larger. Both of these airfoils developed more lift than the others before encountering negative damping, particularly at the higher reduced frequencies.

The unusual shape of the stability boundaries for the HH-02 airfoil is associated with complex changes in its boundary-layer separation characteristics as a function of reduced frequency. Statically and at low frequency, the HH-02 stalled from the trailing edge, but this changed over to leading-edge stall as k increased, with a corresponding change in the shape of the left-hand stability boundary. At higher values of mean angle, its deep stall behavior was very similar to the other three leading-edge stalling airfoils.

Finally, we note that although there appears to be a distinct connection between the type of boundary-layer separation and the size and shape of the instability domain, the pitch damping behavior is not necessarily related to the static-stall behavior. The results of the present investigation, combined with static airfoil tests and theoretical calculations, can serve as a guide in estimating pitch damping characteristics, but an element of uncertainty will remain about the behavior of new airfoil sections until some estimates of their light-stall characteristics are obtained experimentally.

Summary and Conclusions

The results described in the preceding sections provide a basis for reassessing the importance of some of the parameters listed in Table 1 that influence the retreating-blade stall characteristics of helicopter airfoils. Pitch oscillations that simulate the blade element angle-of-attack variations of a rotor in forward flight produce large changes in the stall behavior, and the parameters of this unsteady motion tend to be more important in many cases than the geometry of the blade. Nevertheless, important differences were observed in the two-dimensional dynamic airloads on the various airfoils. Many of these differences could translate into significant differences in performance, vibrations, and aerodynamic stability in rotorcraft applications.

In Fig. 20 we attempt to summarize some of the most important similarities and differences between the seven helicopter airfoils that were studied. Drag divergence Mach number at zero lift in steady flow is one meaningful measure of advancing-blade qualities. Maximum lift capability at moderate Mach number is important on the retreating blade, of course; but in this case, we must decide what limiting conditions to impose, since $C_{L_{max}}$, C_D, and C_M vary with so many parameters besides geometry. This is graphically illustrated by the differences in $C_{L_{max}}$ for static stall, at dynamic stall onset, and in deep stall for a given airfoil. The large values of lift coefficient obtained in deep stall could probably not be utilized in practice because of vibratory loads. However, the results in Fig. 20 show the potential in lifting capability if this problem could be overcome.

Some general observations can be made about the results in Fig. 20. First, all six of the modern helicopter sections offer advantages over the classical NACA 0012 airfoil, as would be expected. Second, the airfoil with the highest lift coefficient for each given set of conditions has the lowest drag-divergence Mach number, and vice versa, also as expected. Third, the airfoils with the better static-stall characteristics tend to exhibit better dynamic stall behavior. However, it is important to note that the increments

between static and dynamic stall lift vary significantly from one profile to another and that the static separation and stall characteristics are not always reliable indicators of dynamic stall behavior.

As we have noted in the previous sections of the paper, the qualitative differences in dynamic stall behavior diminish rapidly as the airfoils penetrate further into the deep-stall regime, which is dominated by the vortex shedding phenomenon. We have also stressed the strong tendency for each airfoil to evolve toward unsteady leading-edge stall as M_∞ increased, at least up to our experimental limit of 0.3, regardless of the quasi-static or low-Mach-number behavior. Furthermore, the transition to leading-edge stall generally occurs as the unsteady conditions take the airfoil into or beyond the light-stall regime, and in the light-stall regime trailing-edge separation generally seems preferable. Consequently, it would seem to be fruitful to concentrate more effort on stall onset and light-stall behavior in the future, both from the standpoint of studying the fundamental phenomena and in trying to develop new and improved rotor-blade sections or high-lift devices. The stall-onset condition is also the one most amenable to theoretical analysis and calculation at the present time.

Finally, we would like to emphasize the importance of transonic flow phenomena in the retreating-blade environment. In the present experiment, many of the changes in stall and separation behavior that occurred as tunnel speed increased coincided with the development of a small supersonic bubble near the leading edge. With or without shock waves, this is a different kind of transonic flow problem than the ones that are currently receiving so much attention by the fluid dynamics community, as indicated in Fig. 21. Further experiments and numerical analysis are urgently needed, particularly at Mach numbers between 0.25 and 0.50, to identify the mechanisms that produce the leading-edge separation and to explore the development of leading-edge shock waves in this unusual situation.

In conclusion, the results of this investigation indicate that further improvements in airfoil performance can be attained in the stall-onset and light-stall regimes, once theoretical methods are developed that include unsteady effects. However, the sensitivity of the dynamic stall airloads to the various parameters of the unsteady motion indicates that accurate prediction of retreating-blade characteristics will continue to depend strongly on an accurate knowledge of the blade-element environment and on accurate correlations of oscillating airfoil data. We hope that the results of our experiment will provide part of this information which is needed to design better rotor blades.

References

1. Lizak, A. A. "Two-Dimensional Wind Tunnel Tests of an H-34 Main Rotor Airfoil Section." TREC Technical Report 60-53, U.S. Army Transportation Research Command, Fort Eustis, Virginia, 1960.

2. Prouty, R. W. "A State-of-the-Art Survey of Two-Dimensional Airfoil Data." Journal of the American Helicopter Society, Vol. 20, No. 4, Oct. 1975, pp. 14-25.

3. Loftin, L. K., Jr., and Smith, H. A. "Aerodynamic Characteristics of 15 NACA Airfoil Sections at Seven Reynolds Numbers." NACA TN-1945, 1949.

4. Gregory, N., Quincey, V. G., O'Reilly, C. L., and Hall, D. J. "Progress Report on Observations of Three-Dimensional Flow Patterns Obtained During Stall Development on Airfoils, and on the Problem of Measuring Two-Dimensional Characteristics." NPL Aero Report 1309. National Physical Laboratory, Teddington, England, 1970.

5. Dadone, L. U. "U.S. Army Helicopter Design Datcom. Volume I - Airfoils." USAAMRDL CR 76-2. U.S. Army Aviation Systems Command, St. Louis, Mo., 1976.

6. Bingham, G. J., Noonan, K. W., and Jones, H. E. "Results of an Investigation of Several New Rotorcraft Airfoils as Related to Airfoil Requirements," in Advanced Technology Airfoil Research, Vol. II, NASA CP-2046, 1979, pp. 109-120.

7. Coulomb, J. "Resultats d'Essais Stationnaires du Profil VR-7," Note Technique. Centre d'Essais Aéronautique de Toulouse, Toulouse, France: 1979.

8. McAlister, K. W., Carr, L. W., and McCroskey, W. J. "Dynamic Stall Experiments on the NACA 0012 Airfoil." NASA TP-1100, 1978.

9. Carr, L. W., McAlister, K. W., and McCroskey, W. J. "Analysis of the Development of Dynamic Stall Based on Oscillating Airfoil Experiments." NASA TN D-8382, 1977.

10. Hicks, R. M., and McCroskey, W. J. "An Experimental Evaluation of a Helicopter Rotor Section Designed by Numerical Optimization." NASA TM-78622, 1980.

11. Balch, D. T. "Helicopter Blade," U.S. Patent No. 3,728,045, 1973.

12. Kemp, L. D. "An Analytical Study for the Design of Advanced Rotor Airfoils." NASA CR-112,297, 1973.

13. Barche, J., ed. "Experimental Data Base for Computer Program Assessment." AGARD AR-138. Advisory Group for Aerospace Research and Development, Neuilly sur Seine, France, 1979.

14. Carr, L. W., and McCroskey, W. J. "A Directionally Sensitive Hot-Wire Probe for Detection of Flow Reversal in Highly Unsteady Flows," in International Congress on Instrumentation in Aerospace Facilities 1979 Record, Sept. 1979, pp. 154-162.

15. McCroskey, W. J., McAlister, K. W., and Carr, L. W. "Dynamic Stall Experiments on Oscillating Airfoils." AIAA Journal, Vol. 14, No. 1, Jan. 1976, pp. 57-63.

16. Allen, H. J., and Vincenti, W. G. "Wall Interference in a Two-Dimensional-Flow Wind Tunnel with Consideration of the Effect of Compressibility." NACA Report 782, 1944.

17. Fromme, J. A., and Golberg, M. A. "Unsteady Two-Dimensional Airloads Acting on Oscillating Thin Airfoils in Subsonic Ventilated Wind Tunnels." NASA CR-2967, 1978.

18. Dadone, L. U. "Two-Dimensional Wind Tunnel Test of an Oscillating Rotor Airfoil." NASA CR-2914, 1977.

19. St. Hilaire, A. L., Carta, F.O., and Jepson, W. D. "The Influence of Sweep on the Aerodynamic Loading of an Oscillating NACA 0012 Airfoil." Paper No. 79-4, American Helicopter Society, 35th Annual National Forum, Washington, D.C., May 1979.

20. Davis, S. S., and Malcolm, G. N. "Unsteady Aerodynamics of Conventional and Supercritical Airfoils." AIAA Paper 80-0734, 1980; also NASA Technical Memorandum in preparation.

21. Gault, D. E. "A Correlation of Low Speed Airfoil Section Stalling Characteristics with Reynolds Number and Airfoil Geometry." NACA TN-3963, 1956.

22. Carta, F. O. "Analysis of Oscillatory Pressure Data Including Dynamic Stall Effects." NASA CR-2394, 1974.

23. Liiva, J., and Davenport, F. J. "Dynamic Stall of Airfoil Sections for High-Speed Rotors." Journal of the American Helicopter Society, Vol. 14, No. 2, Apr. 1969, pp. 26-33.

24. Dadone, L. "Observations on the Dynamic Stall Characteristics of Advanced Helicopter Rotor Airfoils," in Advanced Technology Airfoil Research, Vol. I, NASA CP-2045, Part 2, 1979, pp. 701-715.

25. Ericsson, L. E., and Reding, J. P. "Stall Flutter Analysis." Journal of Aircraft, Vol. 10, No. 1, Jan. 1973, pp. 5-13.

26. Pearcey, H. H., Wilby, P. G., Riley, M. J., and Brotherhood, P. "The Derivation and Verification of a New Rotor Profile on the Basis of Flow Phenomena: Aerofoil Research and Flight Tests," in Aerodynamics of Rotary Wings. AGARD CP-III. Advisory Group for Aerospace Research and Development, Neuilly sur Seine, France, 1972, Paper No. 16.

27. Bauer, F., Garabedian, P., Korn, D., and Jameson, A. "Supercritical Wing Sections II." Lecture Notes in Economics and Mathematical Systems, Vol. 108. Springer-Verlag, Berlin, 1975.

Table 1. Importance of the Dynamic Stall Parameters

Stall parameter	Effect
Airfoil shape	Large in some cases
Mach No.	Small below M ~ 0.2, Large above M ~ 0.2
Reynolds No.	Small(?) at low Mach No., Unknown at high Mach No.
Reduced frequency	Large
Mean angle, amplitude	Large
Type of motion	Virtually unknown
3-D effects	Virtually unknown
Tunnel effects	Virtually unknown

Table 2. Summary of Airfoils Tested

Airfoil	Thickness ratio	Maximum camber	Leading-edge radius	Reference	Remarks
0012	0.120	0	0.0158	5	Reference
Ames-01	0.103	0.014	0.012	10	Optimized for both $C_{L_{max}}$ and M_{DD}
Wortmann FX-098	0.099	0.017	0.007	5	
SC-1095	0.095	0.008	0.008	11	
HH-02	0.096	0.020	0.008	Unpublished	
VR-7 (-3° Tab)	0.119	0.027	0.011	5	High $C_{L_{max}}$
NLR-1	0.086	0.012	0.007	12	High M_{DD}
NLR-7301	0.165	0.017	0.055	13	Supercritical fixed wing

Table 3. Summary of Measured Static Airfoil Characteristics at M = 0.3 and Calculated Drag Divergence Mach Number

Airfoil	C_{L_α}	α_o	C_{M_o}	$C_{D_{min}}$	$X_{a.c.}$	$C_{L_{max}}$	α_{SS}	$(L/D)_{max}$	M_{DD_o}	Small type
0012	0.114	-0.1°	-0.007	0.0072	0.24	1.34	13.7°	90	0.78	Abrupt T.E.*
Ames-01	0.115	-0.6	-0.005	0.0070	0.25	1.46	13.5	100	0.81	Abrupt T.E.
W-098	0.113	-1.3	-0.026	0.0066	0.24	1.44	13.0	94	0.81	Abrupt T.E.
SC-1095	0.114	-0.9	-0.027	0.0073	0.245	1.46	13.5	98	0.80	Mixed
HH-02	0.120	-0.6	0.00	0.0066	0.255	1.44	13.2	92	0.80	T.E.
VR-7	0.121	-1.5	-0.016	0.0071	0.26	1.53	12.5	107	0.75	T.E.
NLR-1	0.107	-1.0	-0.025	0.0071	0.22	1.29	12.3	87	0.86	Abrupt T.E.
NLR-7301	0.121	-1.9	-0.083	0.0078	0.25	1.85	17.8	89	0.75	T.E.

*Trailing edge.

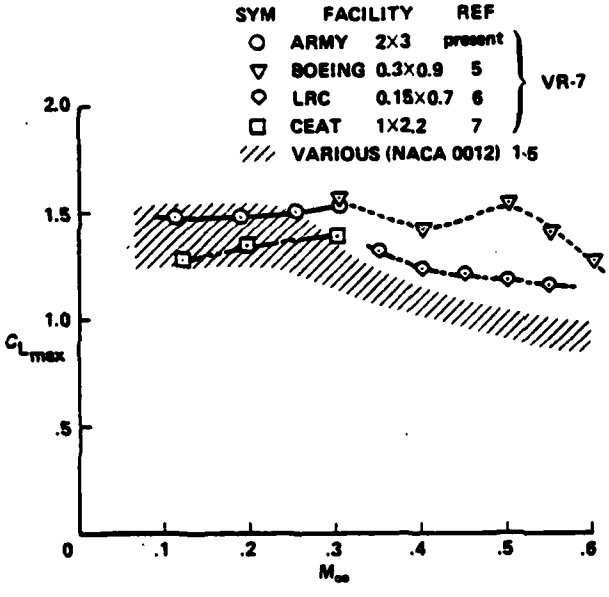

Figure 1. Maximum lift on the NACA 0012 and Vertol VR-7 airfoils measured in steady flow (all tunnel dimensions in meters).

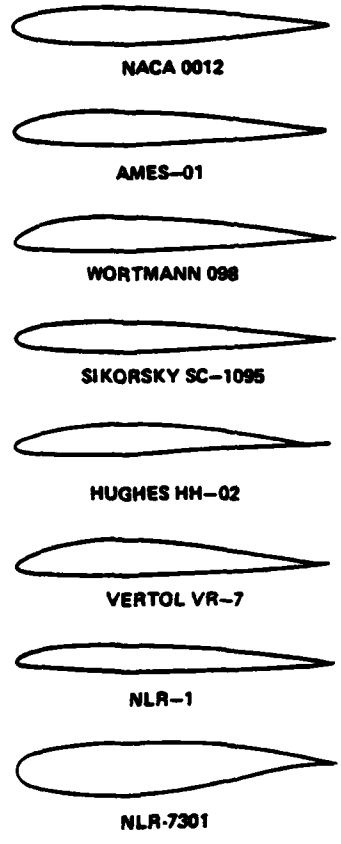

Figure 2. The airfoils tested in the experiment.

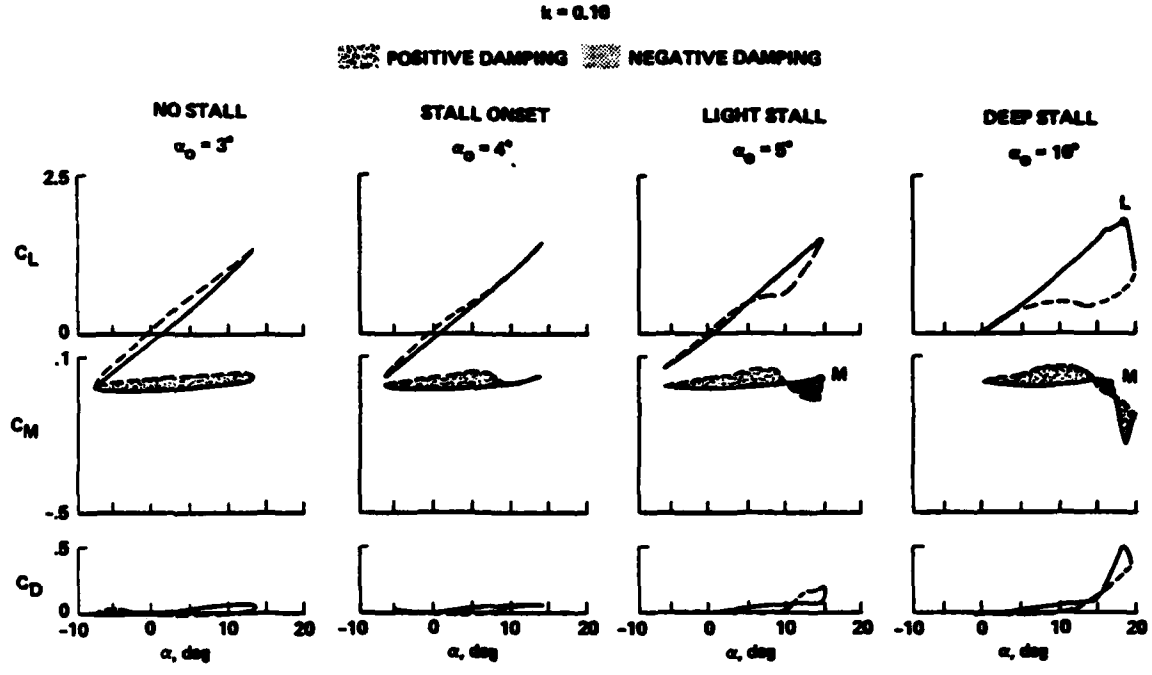

Figure 3. The variation of dynamic-stall airloads with mean angle for the NACA 0012 at M_∞ = 0.3, $\alpha = \alpha_o + 10° \sin \omega t$, and k = 0.10; solid lines denote increasing α.

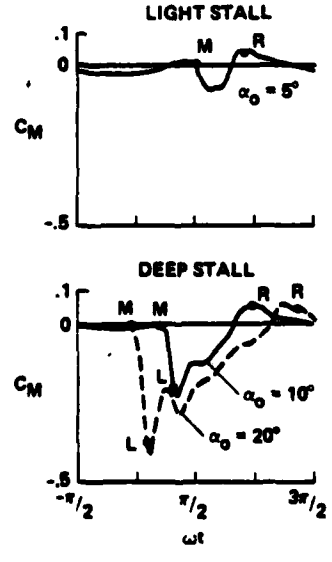

Figure 4. The effect of mean angle on the time history of pitching moment coefficient: NACA 0012 airfoil; M_∞ = 0.3; α_1 = 10°, and k = 0.10.

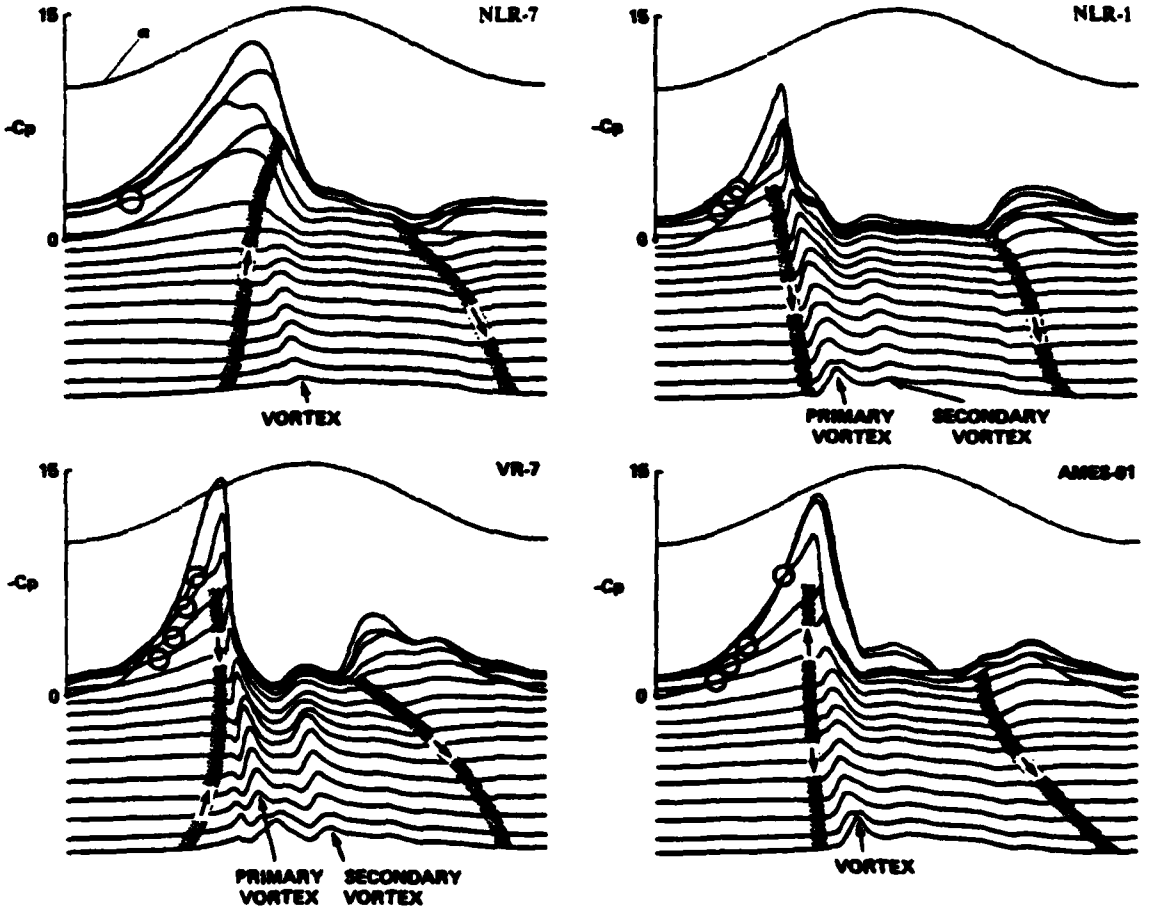

Figure 5. The important stall events for four different types of boundary-layer separation; $M_\infty = 0.25$; $\alpha = 15° + 10° \sin \omega t$; and $k = 0.10$. (Circles indicate laminar bubble.)

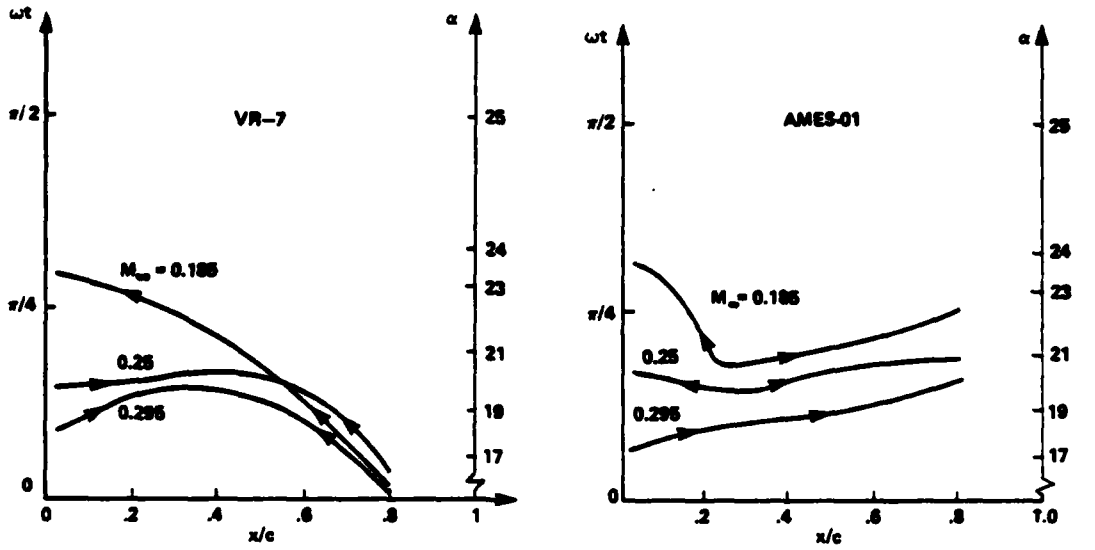

Figure 6. Loci of the initial boundary-layer flow reversal at various Mach numbers for $\alpha = 15° + 10° \sin \omega t$ and $k = 0.10$.

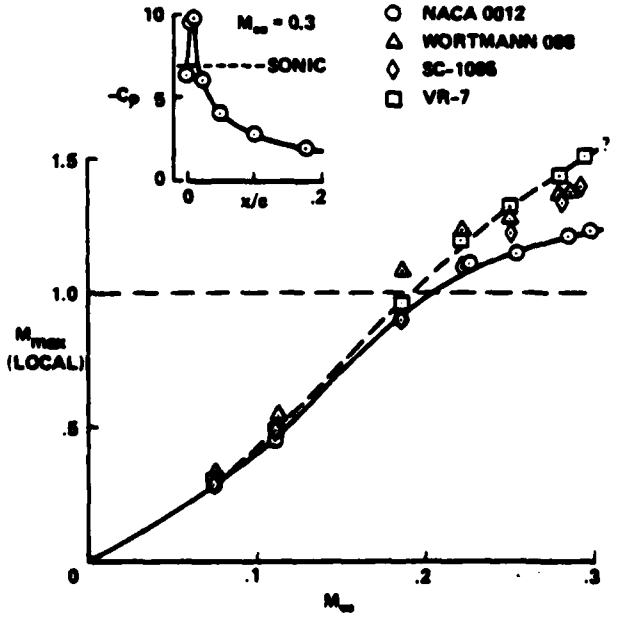

Figure 7. Estimates of the local instantaneous Mach number in the leading-edge region for $\alpha = 15° + 10° \sin \omega t$ and $k = 0.10$.

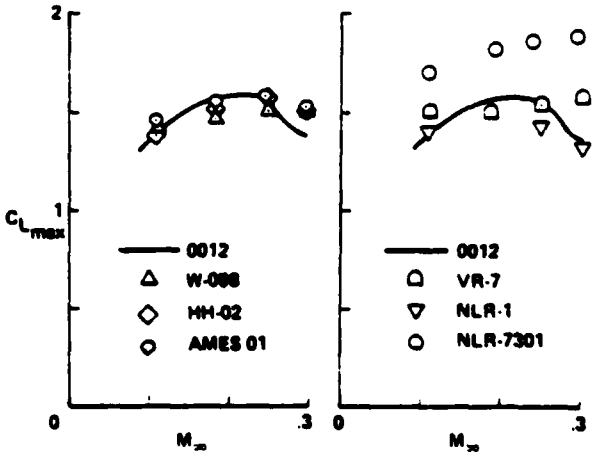

Figure 8. Maximum lift on the various airfoils in steady flow.

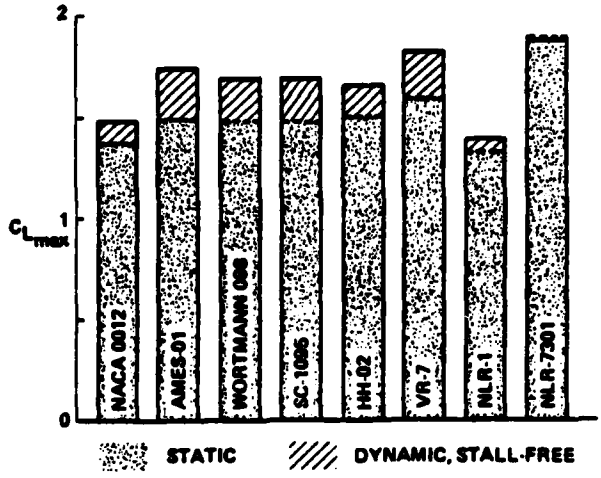

Figure 9. Maximum lift in steady flow and at the dynamic-stall onset condition for $M_\infty = 0.30$, $\alpha = \alpha_o + 10° \sin \omega t$, and $k = 0.10$.

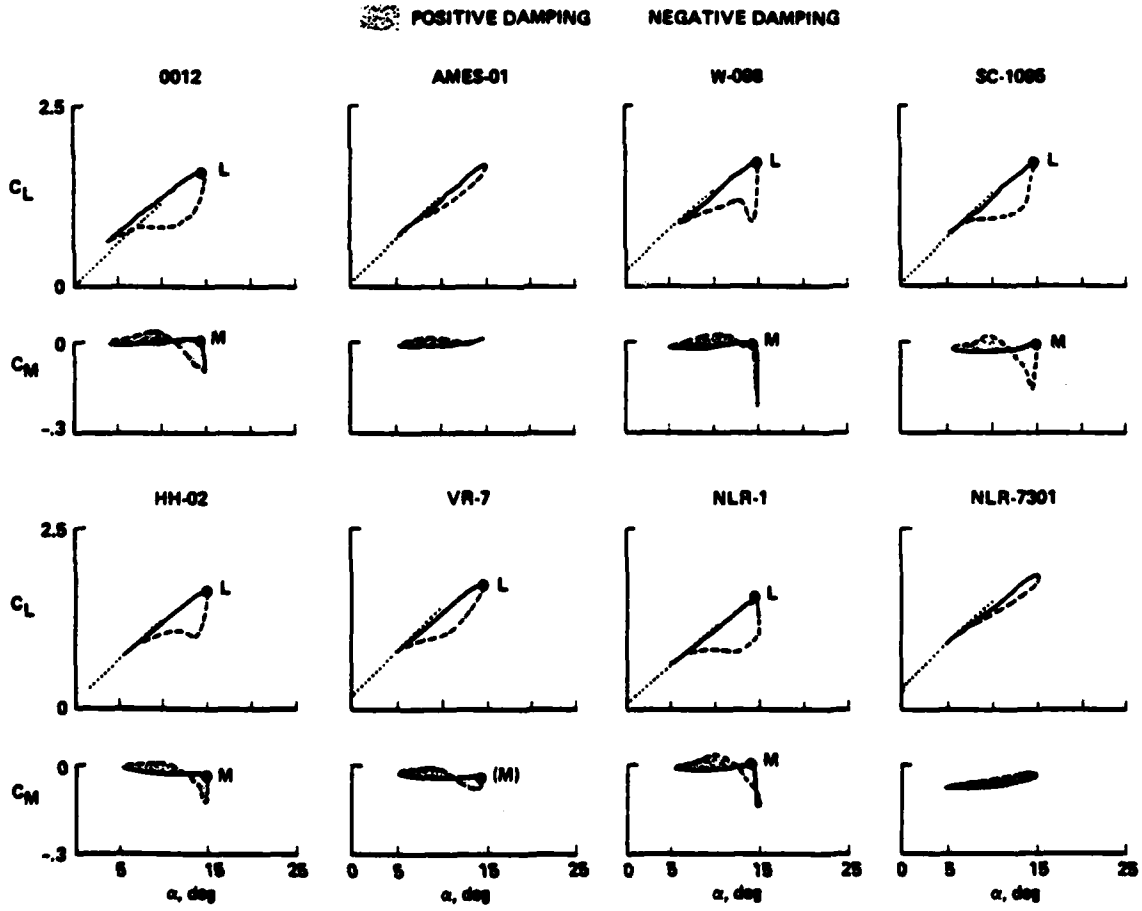

Figure 10. Dynamic airloads in the light-stall regime at $M_\infty = 0.30$, $\alpha = 10° + 5° \sin \omega t$, and $k = 0.10$; solid lines denote increasing α, dotted lines denote static data.

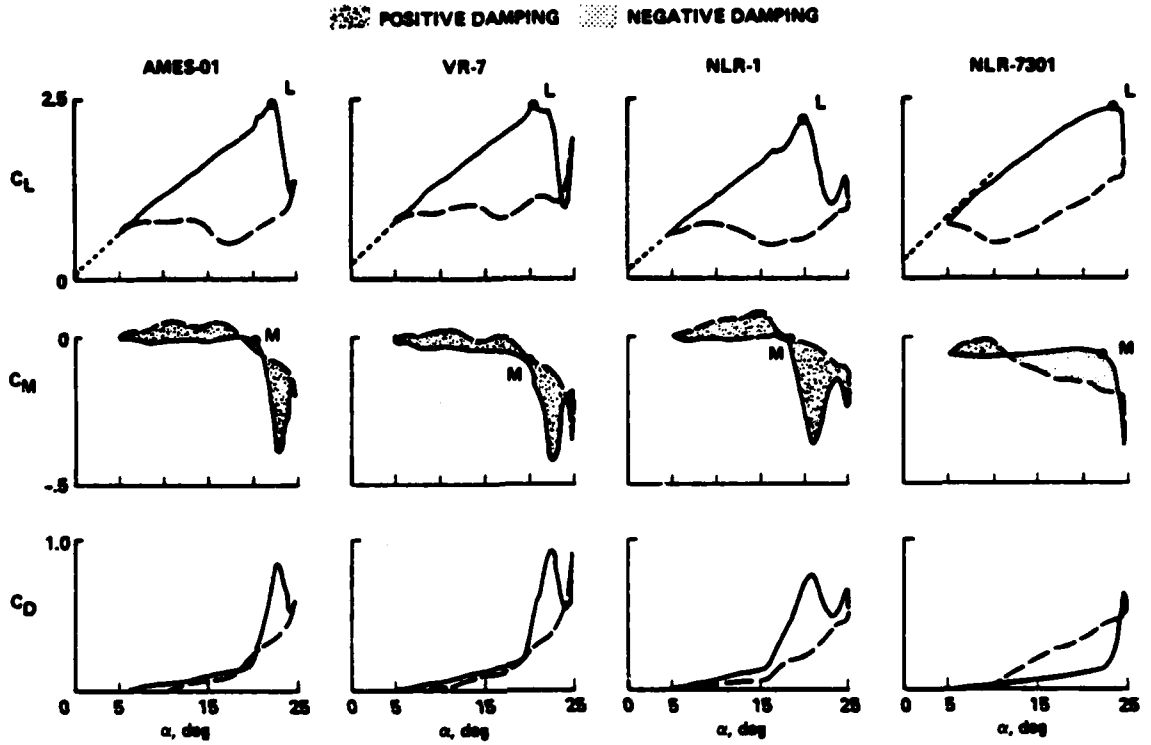

Figure 11. Dynamic airloads in the deep-stall regime at M_∞ = 0.25, $\alpha = 15° + 10° \sin \omega t$, and k = 0.10; short dashed lines denote static data.

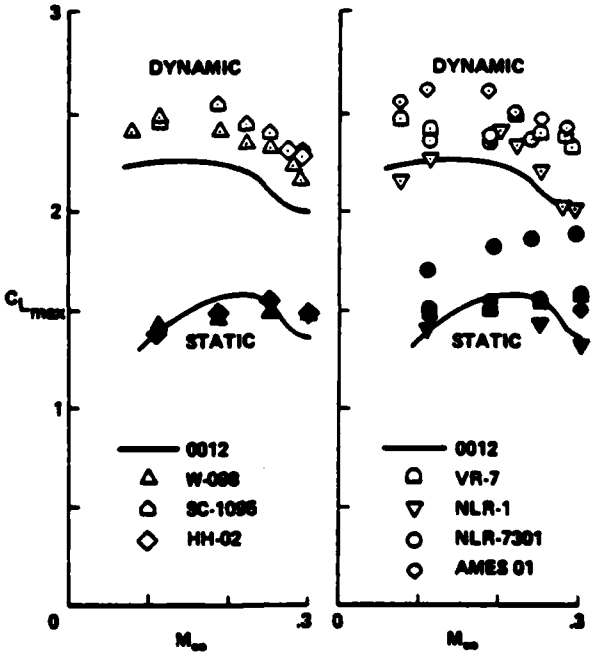

Figure 12. Maximum lift in the deep-stall regime for $\alpha = 15° + 10° \sin \omega t$ and k = 0.10; solid symbols denote static $C_{L_{max}}$.

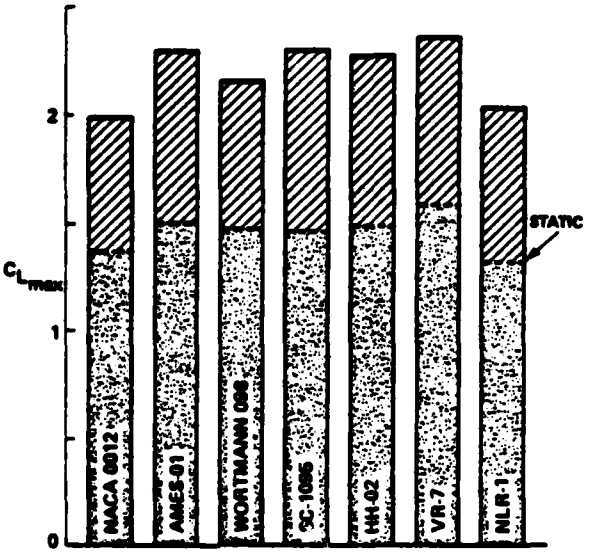

Figure 13. Maximum dynamic lift at $M_\infty = 0.295$, $\alpha = 15° + 10° \sin \omega t$ and $k = 0.10$; dotted lines denote static data.

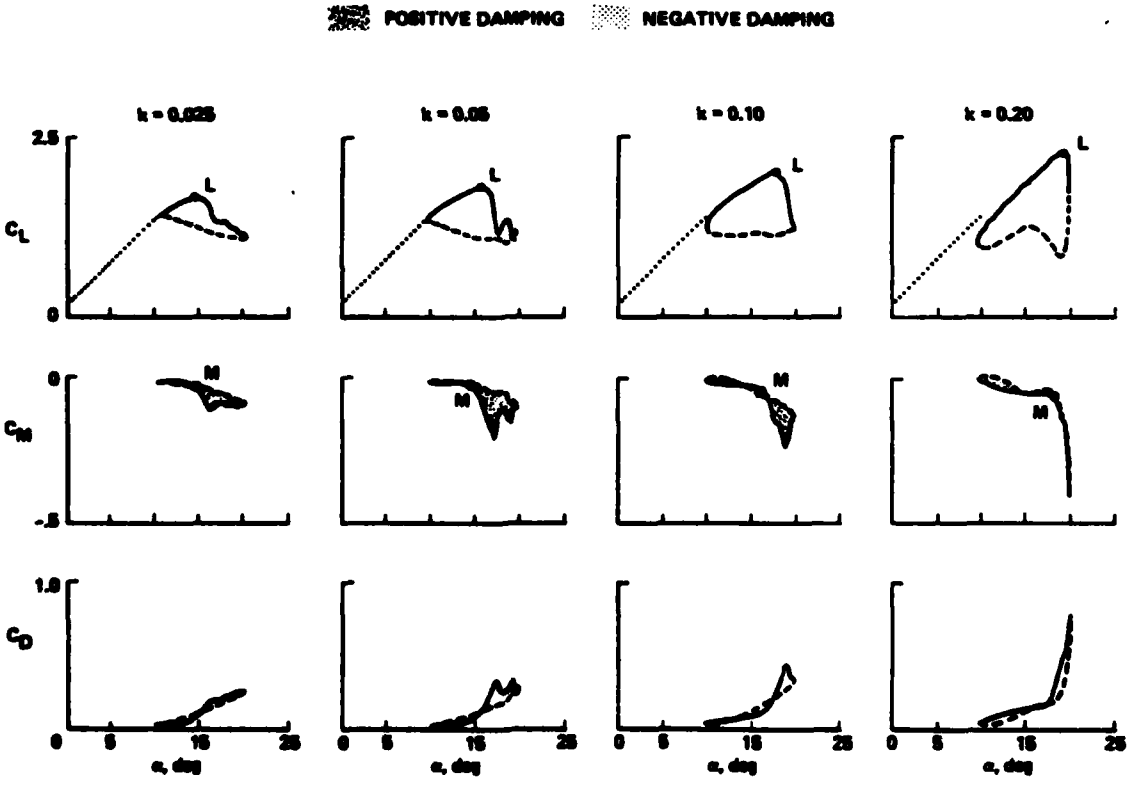

Figure 14. The variation in dynamic airloads on the VR-7 airfoil with reduced frequency. $M_\infty = 0.30$ and $\alpha = 15° + 5° \sin \omega t$.

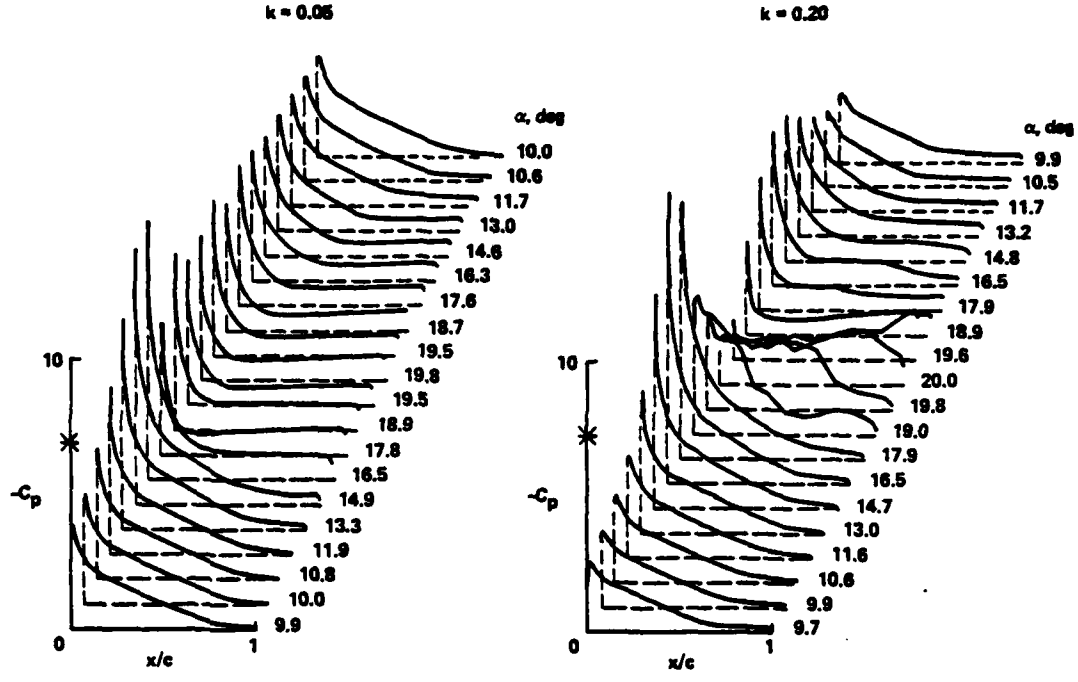

Figure 15. Pressure distributions on the VR-7 airfoil at M_∞ = 0.30 and $\alpha = 15° + 5° \sin \omega t$.

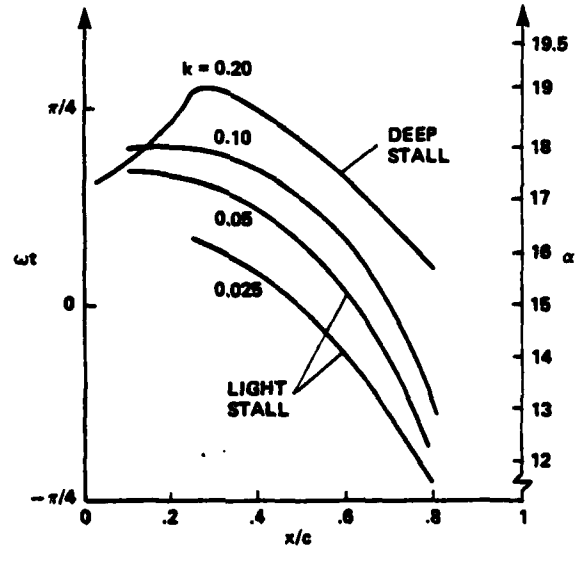

Figure 16. Loci of boundary-layer flow reversal on the VR-7 airfoil at M_∞ = 0.30 and $\alpha = 15° + 5° \sin \omega t$.

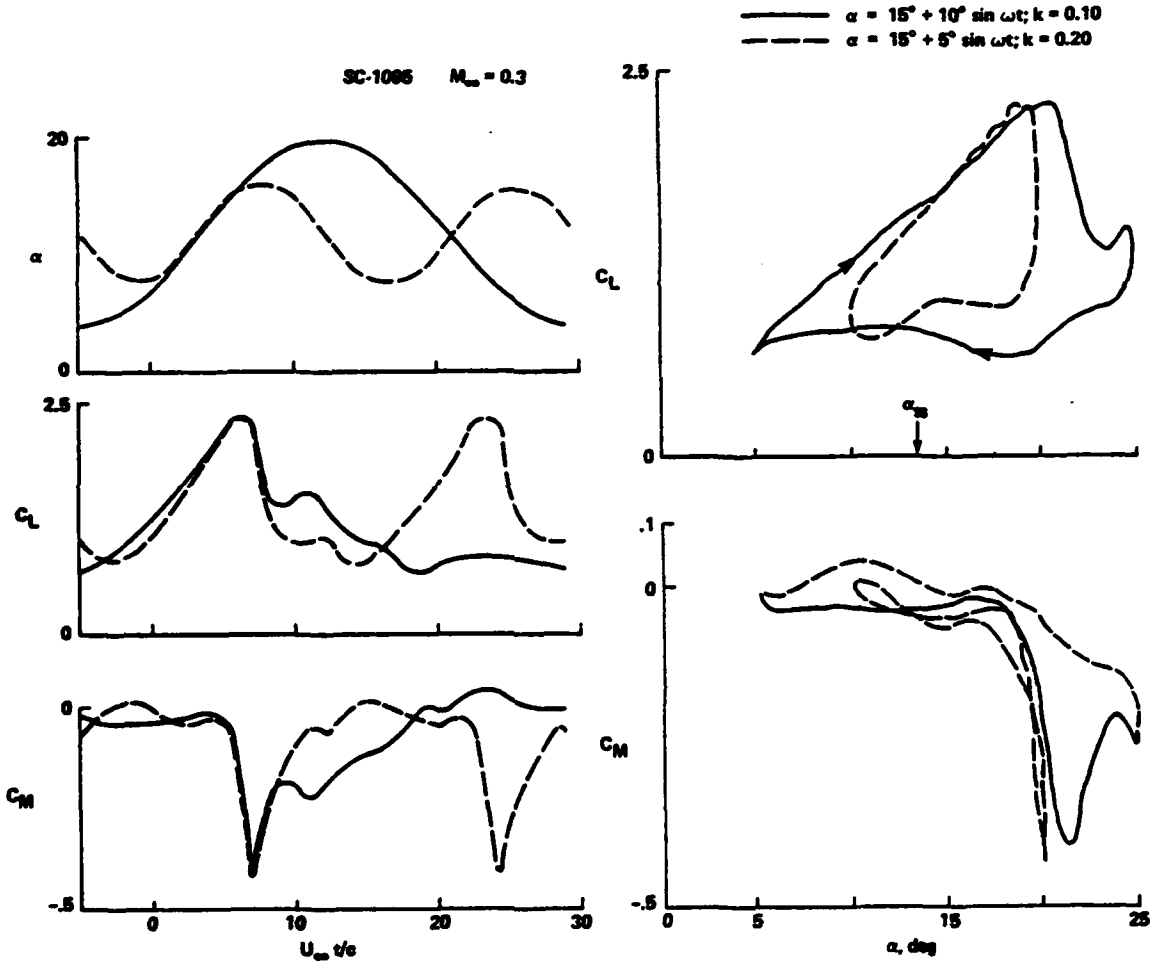

Figure 17. Dynamic airloads on the SC-1095 airfoil for α_o = 15° and $\alpha_1 k$ = 0.17.

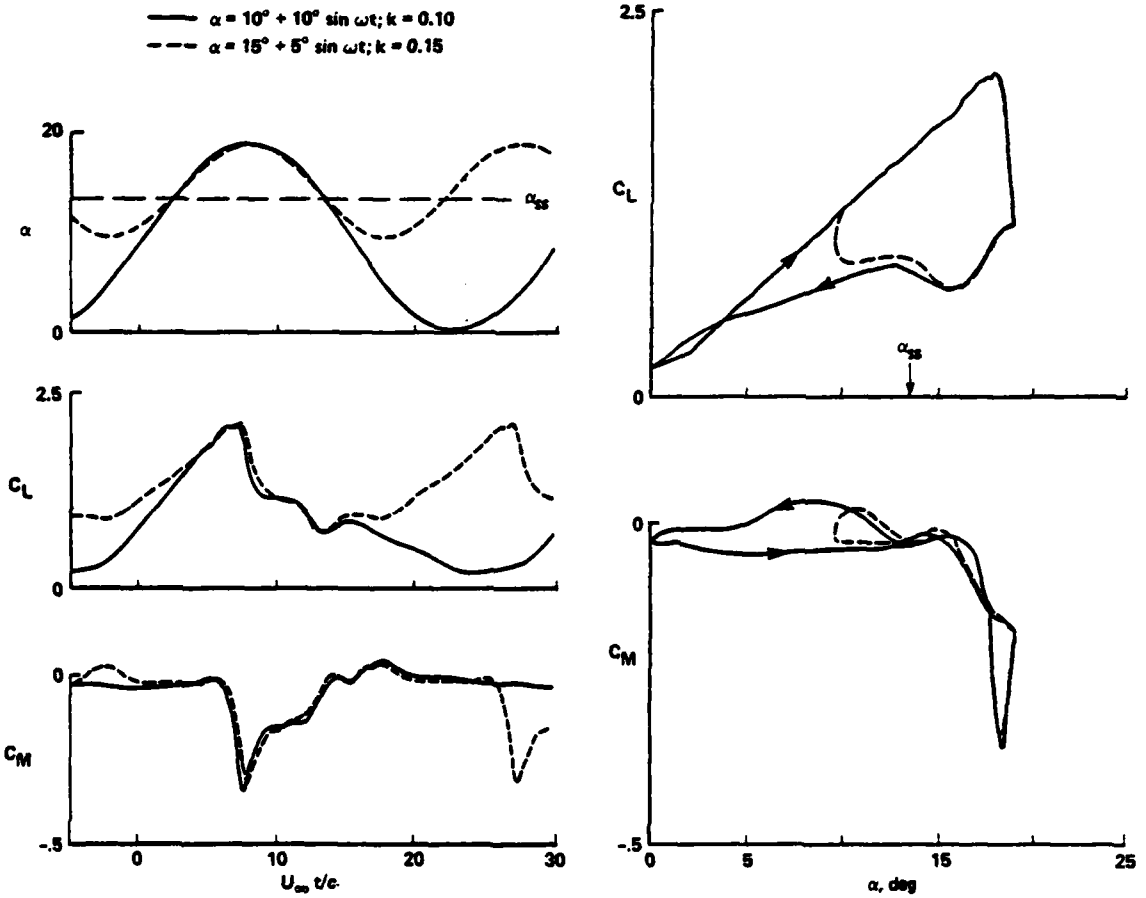

Figure 18. Dynamic airloads on the SC-1095 airfoil for α_{max} = 20° and $\alpha_1 k^2 \simeq 0.002$.

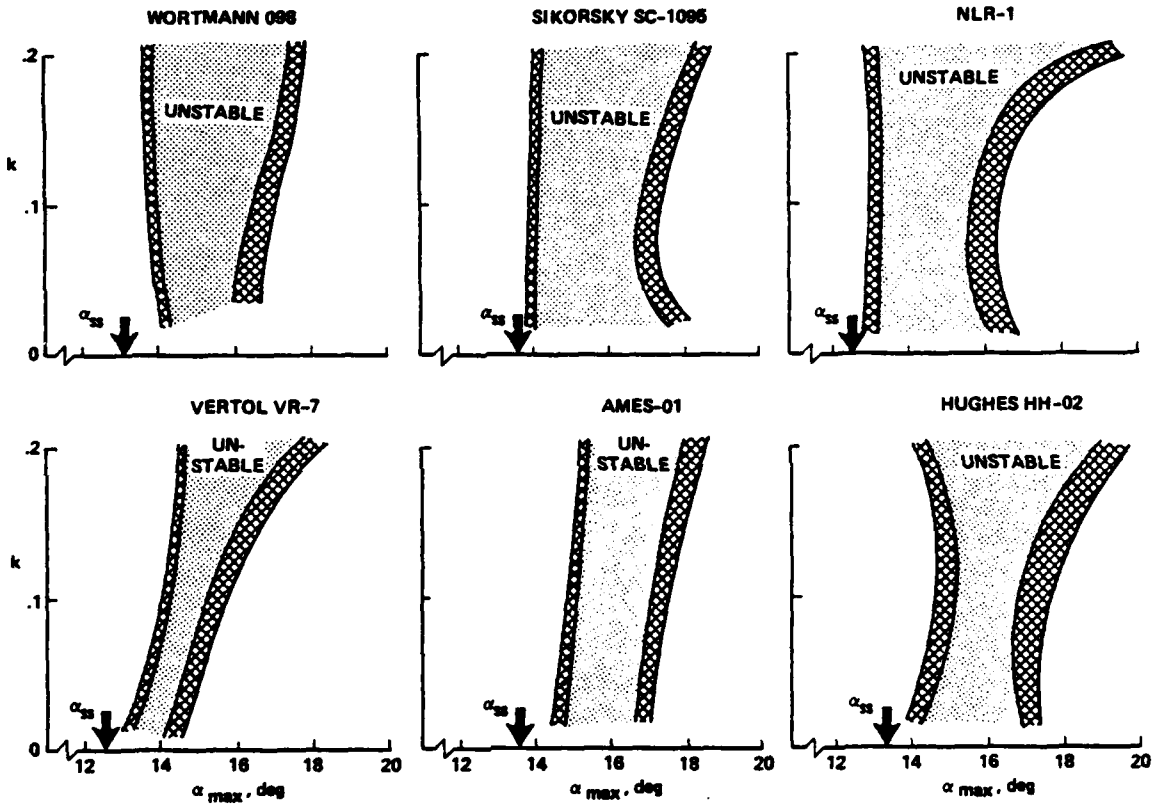

Figure 19. Pitch damping boundaries at $M_\infty = 0.30$ for small amplitude oscillation; crosshatched regions denote $\zeta \simeq 0$.

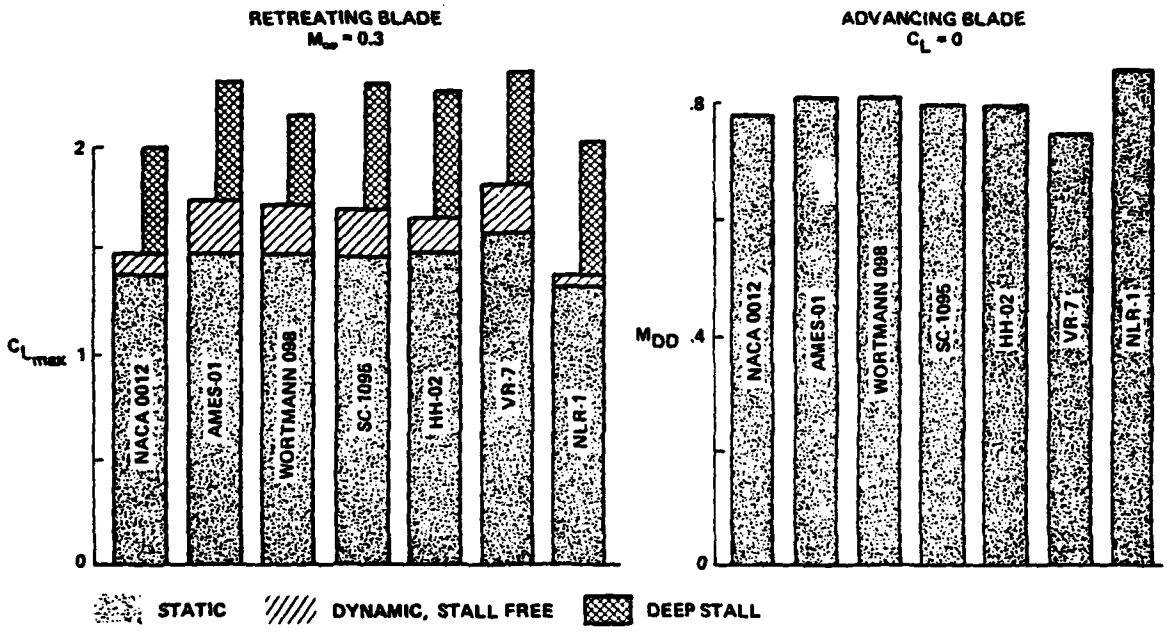

Figure 20. Comparison of retreating and advancing blade characteristics.

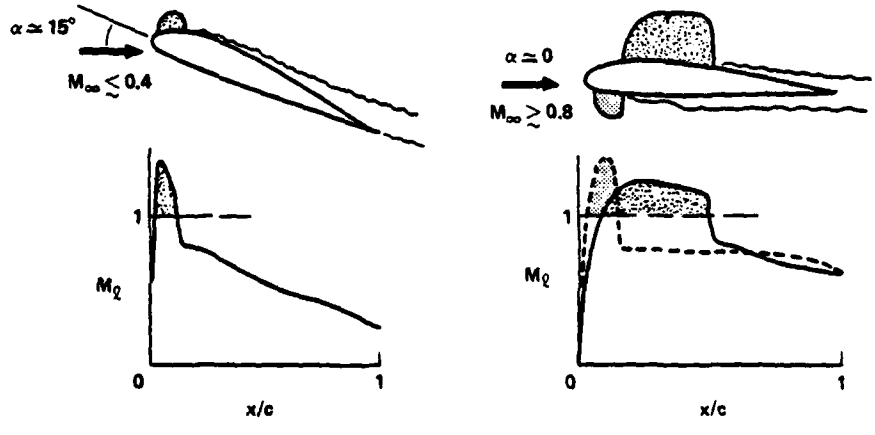

Figure 21. Sketches of transonic flow corresponding to retreating and advancing blade conditions.


TE
MED
8